Space Weather

RESEARCH ARTICLE
10.1029/2021SW002967

Special Section:
Space Weather Impacts on Electrically Grounded Systems at Earth's Surface

Characteristics and Sources of Intense Geoelectric Fields in the United States: Comparative Analysis of Multiple Geomagnetic Storms

Xueling Shi[1,2], Michael D. Hartinger[3], Joseph B. H. Baker[1], Benjamin S. Murphy[4,5], Paul A. Bedrosian[4], Anna Kelbert[5], and Erin Joshua Rigler[5]

[1]Department of Electrical and Computer Engineering, Virginia Tech, Blacksburg, VA, USA, [2]National Center for Atmospheric Research, High Altitude Observatory, Boulder, CO, USA, [3]Space Science Institute, Boulder, CO, USA, [4]U.S. Geological Survey, Geology, Geophysics, Geochemistry Science Center, Denver, CO, USA, [5]U.S. Geological Survey, Geomagnetism Program, Golden, CO, USA

Key Points:

- First multi-storm and multi-station comparative analysis of intense geoelectric fields measured at 1 s cadence
- Interplanetary shocks, ultralow frequency waves, substorms, and interplanetary magnetic field turnings are common sources of intense geoelectric fields
- The causes of intense geoelectric fields differ from storm to storm due to dependence on multiple factors

Supporting Information:

Supporting Information may be found in the online version of this article.

Correspondence to:

X. Shi,
xueling7@vt.edu

Citation:

Shi, X., Hartinger, M. D., Baker, J. B. H., Murphy, B. S., Bedrosian, P. A., Kelbert, A., & Rigler, E. J. (2022). Characteristics and sources of intense geoelectric fields in the United States: Comparative analysis of multiple geomagnetic storms. *Space Weather*, *20*, e2021SW002967. https://doi.org/10.1029/2021SW002967

Received 26 OCT 2021
Accepted 24 JAN 2022

Abstract Intense geoelectric fields during geomagnetic storms drive geomagnetically induced currents in power grids and other infrastructure, yet there are limited direct measurements of these storm-time geoelectric fields. Moreover, most previous studies examining storm-time geoelectric fields focused on single events or small geographic regions, making it difficult to determine the typical source(s) of intense geoelectric fields. We perform the first comparative analysis of (a) the sources of intense geoelectric fields over multiple geomagnetic storms, (b) using 1-s cadence geoelectric field measurements made at (c) magnetotelluric survey sites distributed widely across the United States. Temporally localized intense perturbations in measured geoelectric fields with prominences (a measure of the relative amplitude of geoelectric field enhancement above the surrounding signal) of at least 500 mV/km were detected during geomagnetic storms with Dst minima (Dst_{min}) of less than −100 nT from 2006 to 2019. Most of the intense geoelectric fields were observed in resistive regions with magnetic latitudes greater than 55° even though we have 167 sites located at lower latitudes during geomagnetic storms of $-200\ nT \leq Dst_{min} < -100\ nT$. Our study indicates intense short-lived (<1 min) and geoelectric field perturbations with periods on the order of 1–2 min are common. Most of these perturbations cannot be resolved with 1-min data because they correspond to higher frequency or impulsive phenomena that vary on timescales shorter than that sampling interval. The sources of geomagnetic perturbations inducing these intense geoelectric fields include interplanetary shocks, interplanetary magnetic field turnings, substorms, and ultralow frequency waves.

Plain Language Summary Geomagnetic perturbations related to various phenomena in the near-Earth space environment can induce geoelectric fields within the electrically conducting Earth. The geoelectric field is an important link between phenomena in geospace and geomagnetically induced currents in grounded electricity transmission networks. To investigate sources of hazardous geoelectric fields during geomagnetic storms, we use 1-s geoelectric field measurements that are distributed across the United States. Temporally localized intense perturbations in measured geoelectric fields with prominences of at least 500 mV/km were detected during geomagnetic storms with a Dst minimum of less than −100 nT from 2006 to 2019. Most of these perturbations cannot be resolved with 1-min data because they correspond to phenomena that vary on smaller timescales and higher frequencies. Characteristics and sources of these intense geoelectric fields across multiple geomagnetic storms and multiple geographic regions are investigated.

1. Introduction

The coupling between the solar wind and the magnetosphere-ionosphere (M-I) system generates various phenomena in the near-Earth space environment including M-I currents that generate geomagnetic perturbations. The geomagnetic perturbations can in turn induce geoelectric fields within the electrically conducting Earth. In turn these geoelectric fields drive electric currents that can flow through technological infrastructure in the form of geomagnetically induced currents (GICs). Therefore, the geoelectric field is an important link between magnetospheric/ionospheric phenomena and GICs in grounded electrical transmission networks. Geoelectric fields enable calculation of GICs and both complement and provide validation against direct measurements of GICs, which have limited availability to the scientific community. Moreover, GIC levels depend on specific power

system configurations that change over time, so they are of limited use. Therefore, scientific investigations on the geoelectric field are needed to make tailored engineering assessments specific to particular power grids and other infrastructure. In comparison with globally averaged quantities and regional scale geomagnetic field measurements that have been commonly used for hazard analysis, local activities at smaller spatial scales are best characterized by local geoelectric field measurements. Furthermore, the geoelectric field directly indicates the induction hazard; whereas the commonly used indices (Kp, Dst, dB/dt, etc.) for GIC models do not. Therefore, investigating the sources of intense geoelectric fields in direct measurements helps us gain insights into hazardous GICs that could cause damage to technological infrastructure such as power grids, pipelines, and submarine cables (e.g., Pulkkinen et al., 2017).

Various interplanetary (IP) and M-I sources have been reported to be associated with large geoelectric fields, GICs, or geomagnetic perturbations. Ionospheric current systems in the auroral region during geomagnetic storms and substorms have long been attributed to intense GICs at high and middle latitudes during nighttime (e.g., Freeman et al., 2019; Viljanen, 1997). At low latitude and equatorial regions, equatorial electrojet currents and IP shocks have been reported to induce GICs on the dayside (e.g., Espinosa et al., 2019; Kappenman, 2003; Zhang et al., 2015). Recent studies have shown that geomagnetic pulsations also known as ultralow frequency (ULF: 1 mHz to 1 Hz) waves can drive significant GICs and intense geoelectric fields even at midlatitudes (e.g., Hartinger et al., 2020; Heyns et al., 2021; Yagova et al., 2021). Other causes related to large GICs such as auroral activity (e.g., Apatenkov et al., 2020) and interplanetary magnetic field (IMF) northward and southward turnings (e.g., Tsurutani & Hajra, 2021) have also been reported in recent studies.

In this study, we use direct measurements of geoelectric fields to identify the characteristics and sources of intense geoelectric fields, advancing previous work examining sources of GICs in several ways:

1. We use direct geoelectric field measurements, whereas other studies rely on dB/dt or ΔB as a proxy.
2. We use geoelectric fields rather than GIC measurements for a single type of system. GIC measurements are usually not publicly available and the results cannot be generalized from one type of system configuration to another, whereas the geoelectric field can be used as part of a hazard analysis in any system.
3. We use 1-s geoelectric field measurements that can resolve transient signatures and wave activity with time scales shorter than 1 minute; while others utilize geoelectric field estimates derived from geomagnetic field measurements and Earth conductivity but limit their analysis to 1-min geomagnetic field data. Sometimes uniform Earth conductivity assumption or a one-dimensional layered conductivity model is used when magnetotelluric (MT) transfer functions are not available (e.g., Blanch et al., 2013; Gil et al., 2021).
4. We use multiple stations spread over wide geographic regions during multiple geomagnetic storms, whereas other studies usually focus on small geographic regions during a single geomagnetic storm.

2. Data Sets and Methodology

2.1. Time Series Data

Geoelectric and geomagnetic field measurements at 1-s cadence used in this study are obtained from temporary EarthScope sites, the MT component of the USArray program (Schultz, 2010; Williams et al., 2010). Each EarthScope site measures two horizontal components of the geoelectric fields and all three components of the geomagnetic fields for an approximately 3-week period to obtain the Earth's surface impedance characterizing the relationship between geomagnetic and geoelectric field variations (Kelbert et al., 2019). The measurements are typically made at small arrays of synchronously recording stations that then move to different locations, resulting in a grid sampling of about 70 km across the United States as shown in Figure 1.

OMNI solar wind data (IMF and velocity) and geomagnetic indices (AE and SYM-H) at 1-min resolution obtained from the Coordinated Data Analysis Web (CDAWeb) are used to investigate the upstream solar wind and M-I sources of intense geoelectric fields. Dst data from the World Data Center for Geomagnetism, Kyoto are used to select geomagnetic storms (World Data Center for Geomagnetism, Kyoto et al., 2015). We survey Dst data from 2006 to 2019 when 1-s geoelectric field measurements are available and find 16 storms with a Dst minimum of less than −100 nT ($Dst_{\min} < -100\ nT$) and during which at least six EarthScope sites have geoelectric field measurements. Columns 2–3 in Table 1 show the dates and Dst minimum during each storm. The start date of a storm is identified as the first response in the Dst index, which is usually the increase of the Dst index

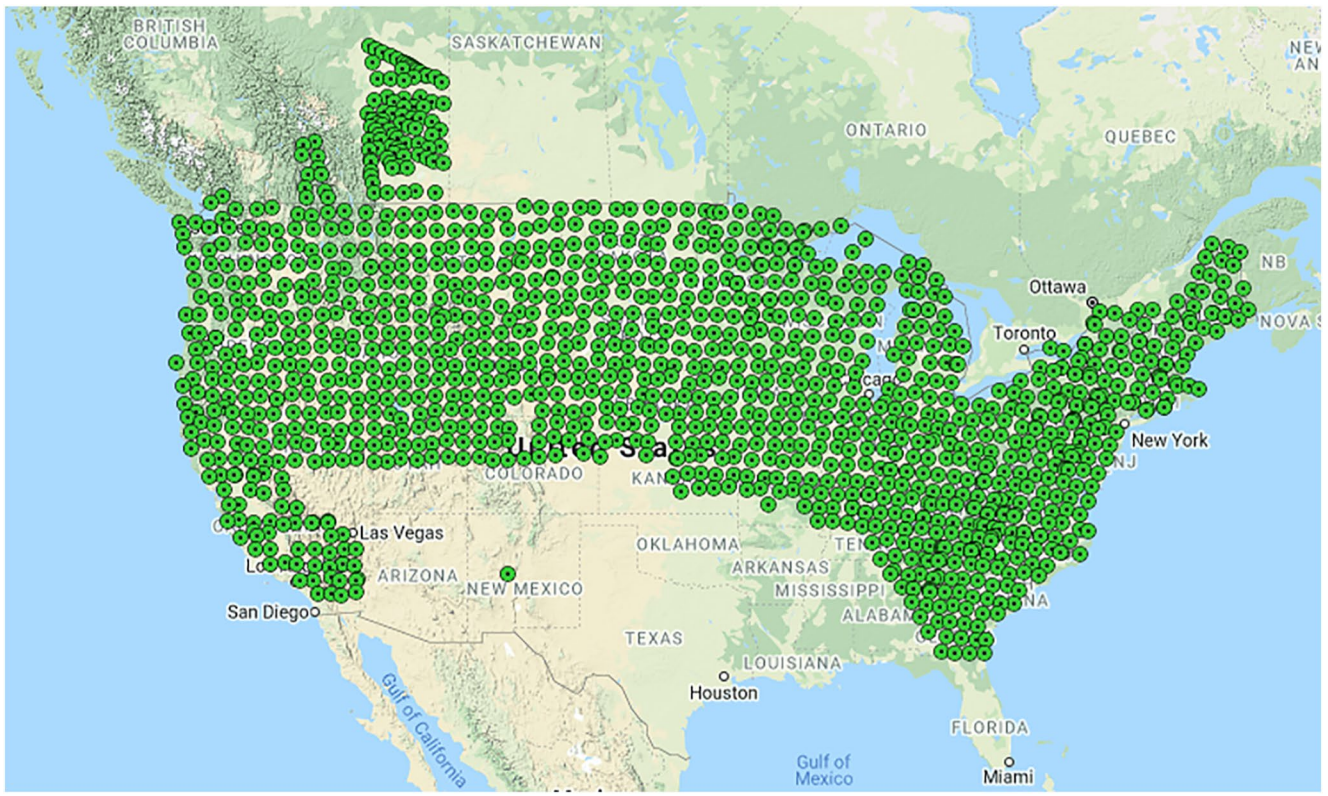

Figure 1. This map shows the location of 1,300 EarthScope and Alberta Array magnetotelluric sites from 2006 to 2019.

Table 1
List of Geomagnetic Storms and Available EarthScope Sites

Event Category	Date	Dst_{min}	Number of Sites
6 storms with large	2011-09-26 to 2011-10-01	−118	16 (6)[a]
geoelectric fields	2011-10-24 to 2011-10-31	−147	12 (5)
($\|E\| \geq 500$ *mV/km*)	2012-07-14 to 2012-07-21	−139	14 (8)
	2013-06-27 to 2013-07-03	−102	14 (1)
	2017-05-27 to 2017-06-01	−125	13 (2)
	2017-09-07 to 2017-09-12	−124	19 (4)
10 null event storms	2011-08-05 to 2011-08-11	−115	21
($\|E\| < 500$ *mV/km*)	2012-09-30 to 2012-10-06	−122	24
	2012-10-07 to 2012-10-12	−109	28
	2013-05-31 to 2013-06-06	−124	15
	2015-06-21 to 2015-06-28	−204	12
	2015-10-06 to 2015-10-12	−124	6
	2015-12-19 to 2015-12-26	−155	12
	2015-12-31 to 2016-01-04	−110	8
	2016-10-12 to 2016-10-16	−104	20
	2018-08-25 to 2018-08-31	−174	10

[a]Shown in the parenthesis is the number of sites that detected intense geoelectric fields.

in response to a compression of the magnetosphere caused by an IP shock. The storm end date is identified when the Dst index recovers to the pre-storm values or as the seventh day from the start date if it takes more than 7 days for the Dst index to recover to pre-storm values. The duration of each storm ranges from four to seven days with an average duration for all 16 storms of 5.75 days. The last column in Table 1 shows the number of available EarthScope sites that had at least one full day recording for each geomagnetic storm and the number of sites (in the parenthesis) that detect intense geoelectric fields using the algorithm described below. Note that not all sites had measurements throughout a geomagnetic storm, the average recording time of all available sites during 16 storms is about 4.6 days.

2.2. Geoelectric Field Peak Detection Algorithm

The *scipy. signal.find_peaks* (Virtanen et al., 2020) function is used to find peaks/valleys in geoelectric field measurements for two horizontal components E_x (geographic north-south) and E_y (geographic east-west). This function finds all local maxima by comparing neighboring values in a 1-D array. To find both peaks and valleys, the function operates on the absolute values of the geoelectric field data. Hereafter, we call each identified event as a "peak" for the sake of convenience. A peak is detected if it meets the following criteria: (a) it must be topologically prominent above the surrounding signal by at least 500 mV/km (i.e., $|E|_{prominence} \geq 500$ *mV/km*); (b) it must have a minimum width of 3 s; and, (c) it must be separated from an adjacent peak by at least 30 s (Arritt, 2020).

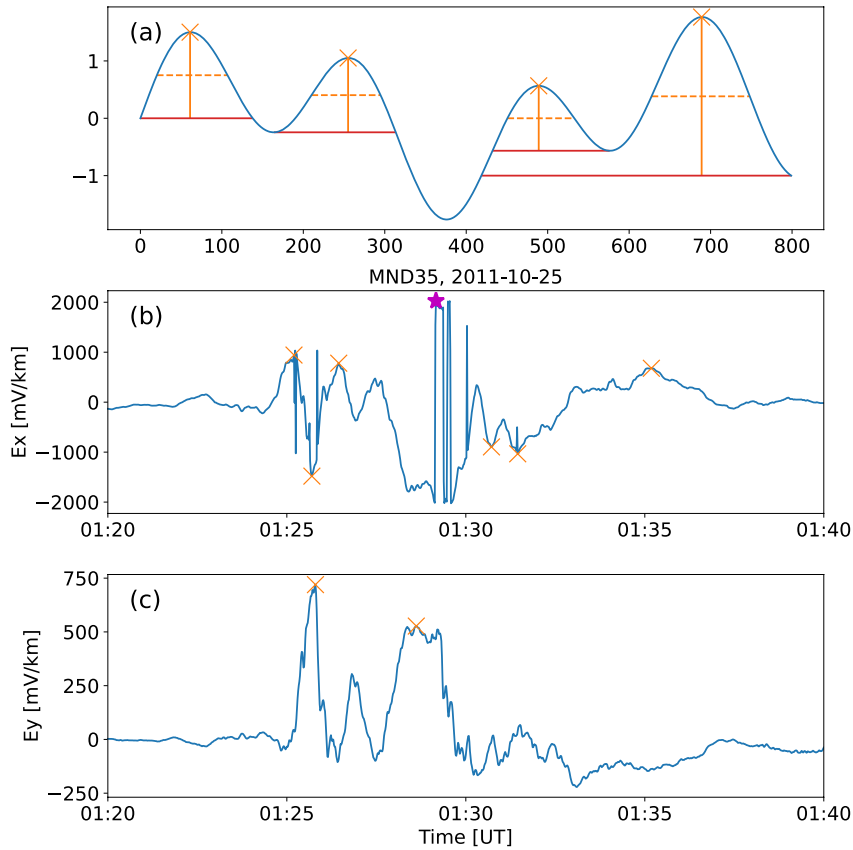

Figure 2. Example of peaks identified using the algorithm described in the text. (a) Idealized example of peaks (orange crosses) with prominences of at least 1. Vertical orange line indicates the prominence of the peak. Horizontal orange dashed and red solid lines indicate the width and the lowest contour line of the peak, respectively. Event example of geoelectric field peaks/valleys identified in the (b) E_x and (c) E_y component at site MND35 from 01:20 to 01:40 UT on 25 October 2011. Orange crosses and magenta stars are identified peaks/valleys and bad data values, respectively.

An idealized example of peaks (marked as orange crosses) with prominences of at least one is shown in Figure 2a. Note that the prominence of a peak (vertical orange lines in Figure 2a) is not necessarily the same as the absolute value of the peak. The prominence is calculated as the vertical difference between the peak's height itself and its lowest contour line (horizontal red lines in Figure 2a), which is defined as follows:

1. Extend a horizontal line from the present peak to the left and right until the line either reaches the window border or intersects the signal again at the slope of a higher peak. An intersection with a peak of the same height is ignored.
2. On each side find the minimal signal value within the interval defined above. These points are the peak's bases. The higher of the two bases marks the peak's lowest contour line.

The width of a peak (horizontal orange dashed lines in Figure 2a) is then defined at half the prominence height. One event example of intense geoelectric fields identified using the algorithm described above is shown in Figures 2b–2c. Note for real events, unlike the idealized example in Figure 2a, the function operates on the absolute values of the geoelectric field data to find both peaks and valleys. In total, seven peaks/valleys were identified in the E_x component (Figure 2b) and two in the E_y component (Figure 2c). The only outlier marked as a magenta star in the E_x component is a bad data value in the geoelectric field measurements. All identified geoelectric field events are visually inspected, outliers and artifacts (such as the one shown in Figure 2b as a magenta star) that cannot be filtered using the above algorithm are manually removed.

3. Statistics of Intense Geoelectric Fields

The geoelectric field peak detection algorithm described in the last section was applied to data collected at 203 EarthScope sites during the 16 geomagnetic storms listed in Table 1. The storms are sorted into two categories: storms with intense geoelectric fields and null event storms as shown in Column 1 of Table 1. One reason some strong storms lack signatures of intense geoelectric fields (e.g., $Dst_{\min}$ of −204 nT in June 2015 and −174 nT in August 2018 are null event storms) is because we are not sampling the same local conditions during each event - for example, some of the more extreme storms might have occurred when EarthScope sites were located at low latitudes or regions of low lithospheric resistivity. Figure 3 shows the location of (a) 203 available EarthScope sites during 16 geomagnetic storms and (b) 24 EarthScope sites where intense geoelectric fields were actually identified. All sites are color coded with the Berdichevsky average apparent resistivity (Berdichevsky & Dmitriev, 1976) at the period of ∼500 s. Note that blue (red) dots indicate resistive (conductive) regions. The available EarthScope data were from sites located in the eastern and central United States and below 58° magnetic latitude (MLAT) (red dashed line at the top in Figure 3a). The 24 sites that observed intense geoelectric fields were located in the upper midwest and northeastern United States and all within resistive regions (blue dots in Figure 3b). Most of these sites were located above 55° MLAT (red dashed line at the bottom). The novelty of the EarthScope data used in this study is direct measurements of geoelectric and magnetic fields spread over wide geographic regions (Figures 1 and 3a). This enables investigation of a more comprehensive picture of the causes of intense geoelectric fields because we examine more than one storm and in a range of geologic settings using direct measurements of geoelectric fields.

In total, 361 intense geoelectric field peaks were identified in data collected at 24 EarthScope sites during six geomagnetic storms, of which, 130 peaks were identified in the E_x (north-south) component (Figure 4a) and 231 peaks were identified in the E_y (east-west) component (Figure 4b). Width versus prominence of the detected intense geoelectric field peaks are shown in Figure 4. Most events have a prominence less than 1,000 mV/km and a width less than 200 s (Figure 4c). Extreme events can have a prominence up to 1,000–2000 mV/km, comparable to the thresholds commonly used to identify hazardous events (Lucas et al., 2020). Note that 73.4% of the events have a width less than 60 s and thus are difficult to resolve with 1-min resolution data. The event list with information on the properties of each peak is provided in Zenodo (https://doi.org/10.5281/zenodo.6338092).

We next examine how reliable dB/dt is as a proxy for geoelectric fields. The corresponding $|dB_x/dt|$ (top panels) and $|dB_y/dt|$ (bottom panels) of intense geoelectric field events as a function of the prominence for the E_x component (left) and the E_y component (right) are shown in Figure 5. Geoelectric field peaks in the E_x (E_y) component are generally associated with larger $|dB_y/dt|$ ($|dB_x/dt|$), that is, more large $|dB/dt|$ events ($|dB/dt| > 2\ nT/s$) are shown in Figures 5b and 5c; while most $|dB/dt|$s have values less than 2 nT/s (red horizontal dashed line) in Figures 5a and 5d. The fact that some large $|dB/dt|$s are also seen in Figures 5a and 5d indicates that geoelectric fields and dB/dt are not strictly orthogonal, which is consistent with realistic three-dimensional (3D) Earth conductivity. Note that the intense geoelectric fields were detected from 24 EarthScope sites that are all quite resistive (Figure 3b), although there are other resistive sites at lower latitudes that did not detect intense geoelectric fields (Figure 3a). This result shows that dB/dt is not always a reliable indicator of intense geoelectric fields, which depend on multiple factors including Earth conductivity and sources that drive them (J. J. Zhang et al., 2020), which will be discussed in the next section.

We also examine the spatial distribution of these intense geoelectric fields. Figure 6a shows the MLAT versus magnetic local time (MLT) distribution of all events. Both dayside and nightside events were observed with a concentration of intense geoelectric fields in the post-midnight sector. The upper limit in the MLAT (first red horizontal dashed line on the top) is caused by a lack of data coverage at higher latitudes (Figures 3a and 6b). By contrast, the lower limit in MLAT (second red horizontal dashed line) is physical because we have 167 EarthScope sites located at MLAT <55° (Figure 6b) but very few events were identified (Figure 6a). This indicates that intense geoelectric fields are generally rare at MLAT <55° during storms for which $-200\ nT \le Dst_{\min} \le -100\ nT$.

4. Sources of Intense Geoelectric Fields

To investigate typical sources of intense geoelectric fields during geomagnetic storms, we visually inspected all the peaks in a format as shown in Figure 7, which includes (a-b) IMF and solar wind velocity from OMNI, (c-f) two horizontal components of geoelectric and geomagnetic fields from an EarthScope site, (g) AE index, and (h)

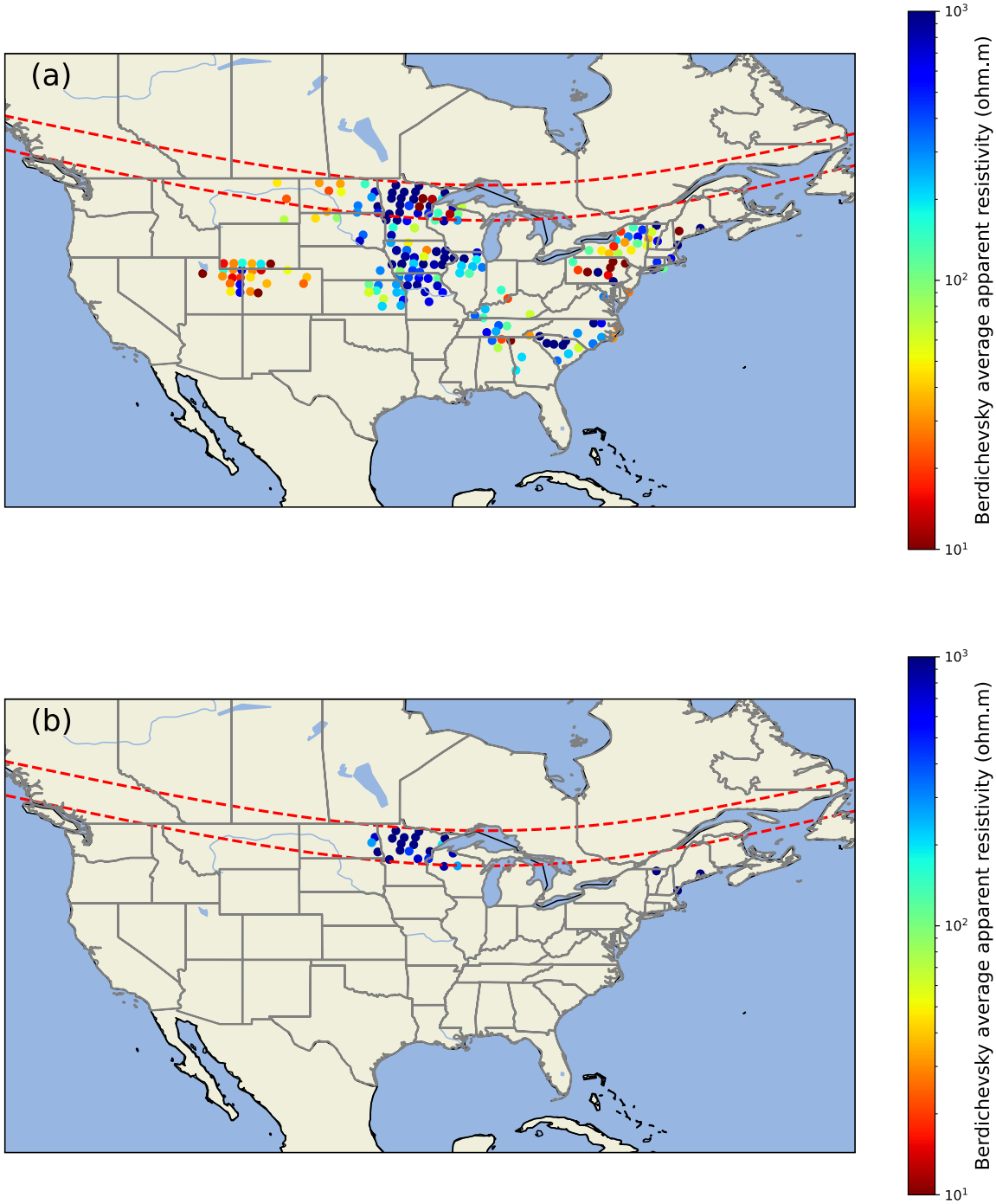

Figure 3. Spatial distribution of (a) 203 available EarthScope sites during the 16 geomagnetic storms; (b) 24 EarthScope sites that detected intense geoelectric fields during geomagnetic storms. The red dashed lines from top to bottom indicate MLAT of 58° and 55°, respectively.

SYM-H index. Figure 7 shows an example summary plot during the 24–25 October 2011 storm, which was driven by a coronal mass ejection as reported by Blanch et al. (2013) and Zou et al. (2013). We only show observations from the first two days of the storm because intense geoelectric fields were detected on both days at site MND35. The IP shock arrived at the Earth around 18:31 UT on 24 October 2011 (Figures 7a and 7b and other upstream satellite measurements not shown) and caused the storm sudden commencement (SSC), which can be identified from ground magnetometer measurements (Figures 7e and 7f) and SYM-H index (Figure 7h). The first two peaks in the E_x component are identified to be associated with the IP shock due to the closely coincident timing

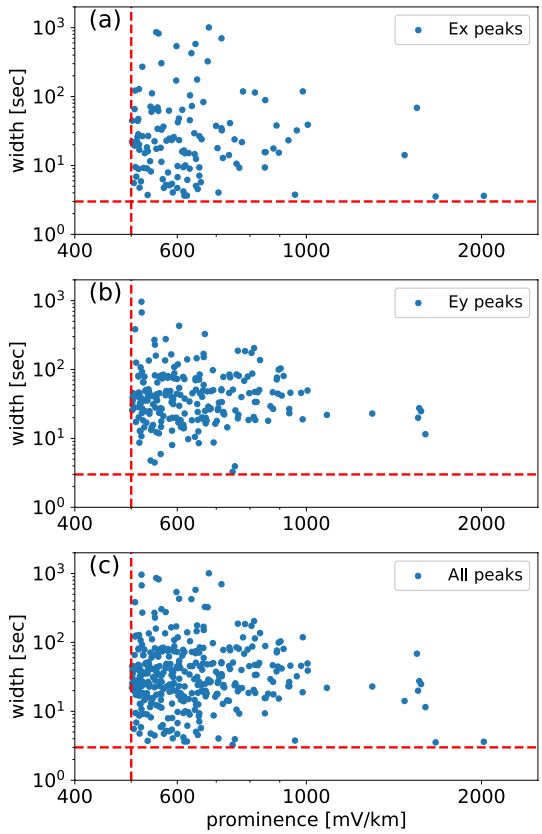

Figure 4. Distribution of geoelectric field peak width versus prominence for (a) the E_x component, (b) the E_y component, (c) both components. The red vertical and horizontal dashed lines indicate the minimum prominence of 500 mV/km and the minimum width of 3 s, respectively.

with the SSC. The second group of geoelectric field peaks in both E_x and E_y components are identified to be associated with an IMF turning (Figure 7a). Large magnetic field perturbations are also observed after the IMF turning (Figures 7e and 7f). More details on the association of intense geoelectric fields with possible sources will be analyzed later in the paper.

After meticulous inspection of all geoelectric field peaks, we categorised the sources into five classes: IP shock (C1), IMF turning (C2), substorm (C3), ULF wave (C4), and others (C5). Table 2 summarizes these potential sources associated with the intense geoelectric field events during six geomagnetic storms using the the algorithm described in Section 2.2. Storm date in the first column is defined to be the date when the Dst index reached its minimum value during the storm. For each source category, multiple EarthScope sites usually observed the same phenomenon at approximately the same time. For ULF wave and substorm related sources, multiple geoelectric field peaks were usually identified from one site. The UT time and corresponding MLT for the first peak from one site are listed for each category. For some categories, when multiple peaks from multiple sites were identified, a time interval in UT and MLT is then provided. When there is no obvious source identified or further investigation is needed to confirm a source, we classify them as others (C5). Event examples for each category are shown in the following subsections.

4.1. IP Shock

The impact of an IP shock causes what is known as a sudden impulse (SI) observed by ground magnetometers or an SSC if followed by a geomagnetic storm (Joselyn & Tsurutani, 1990). Figure 8 is a zoomed-in version of the data shown in Figure 7 centered on the IP shock arrival at ~18:31 UT. As reported in Blanch et al. (2013), upstream satellites including WIND, ACE, and THEMIS B observed the IP shock at 17:39, 17:48, and 18:22 UT, respectively. The first intense geoelectric field event was observed at 18:31:41 UT by the MND35 site, which was located at Tidd Lake, Minnesota. This peak has a prominence of 1,670 mV/km and a width of 3.5 s. The corresponding dB_x/dt and dB_y/dt are −5.910 nT/s and −5.160 nT/s, respectively. A similarly intense geoelectric field peak can be identified in the MNE35 site at 18:31:41 UT (not shown). Both sites were located around local noon when the IP shock impinged on the Earth's magnetosphere (see Table 2 for MLT information). These transient intense geoelectric fields cannot be resolved in 1-min resolution geoelectric and geomagnetic field data. Note the second peak observed at 18:32:26 UT is associated with IP shock driven ULF waves and the properties of this category are different from the IP shock direct driven transient peak as discussed above. Details on ULF wave related intense geoelectric fields will be discussed in a later section.

Blanch et al. (2013) also calculated the geoelectric fields in the Catalan sector (northeastern Spain) on 24–25 October 2011 using the plane wave assumption and uniform Earth conductivity. They found the E_y component with an amplitude of 100–150 mV/km was much larger than the E_x component during the SSC. While the event at 18:31 UT showed approximately equal dB/dt in both x and y directions, for the two EarthScope sites in Minnesota (MND35 and MNE35), it is the E_x component that had a larger amplitude (Figures 8c and 8d) due to 3D realistic Earth conductivity. These sites showed pronounced enhancement in the E_x response due to their location atop electrically resistive granite and adjacent to a conductive sulfide-rich basin (Bedrosian, 2016; Murphy et al., 2021). This 3D subsurface conductivity distribution gives rise to pronounced current channeling and is the ultimate cause of the asymmetry in the measured geoelectric fields. For the other three storms with intense geoelectric fields observed in association with an IP shock as shown in Table 2, it is the E_y component that dominated, although two sites also observed intense geoelectric fields in the E_x component. It is common to assume an idealized driver like an IP shock generates perturbations only in the north-south component of the magnetic field at mid- and low-latitudes. In this idealized scenario, if we assume uniform Earth conductivity, that

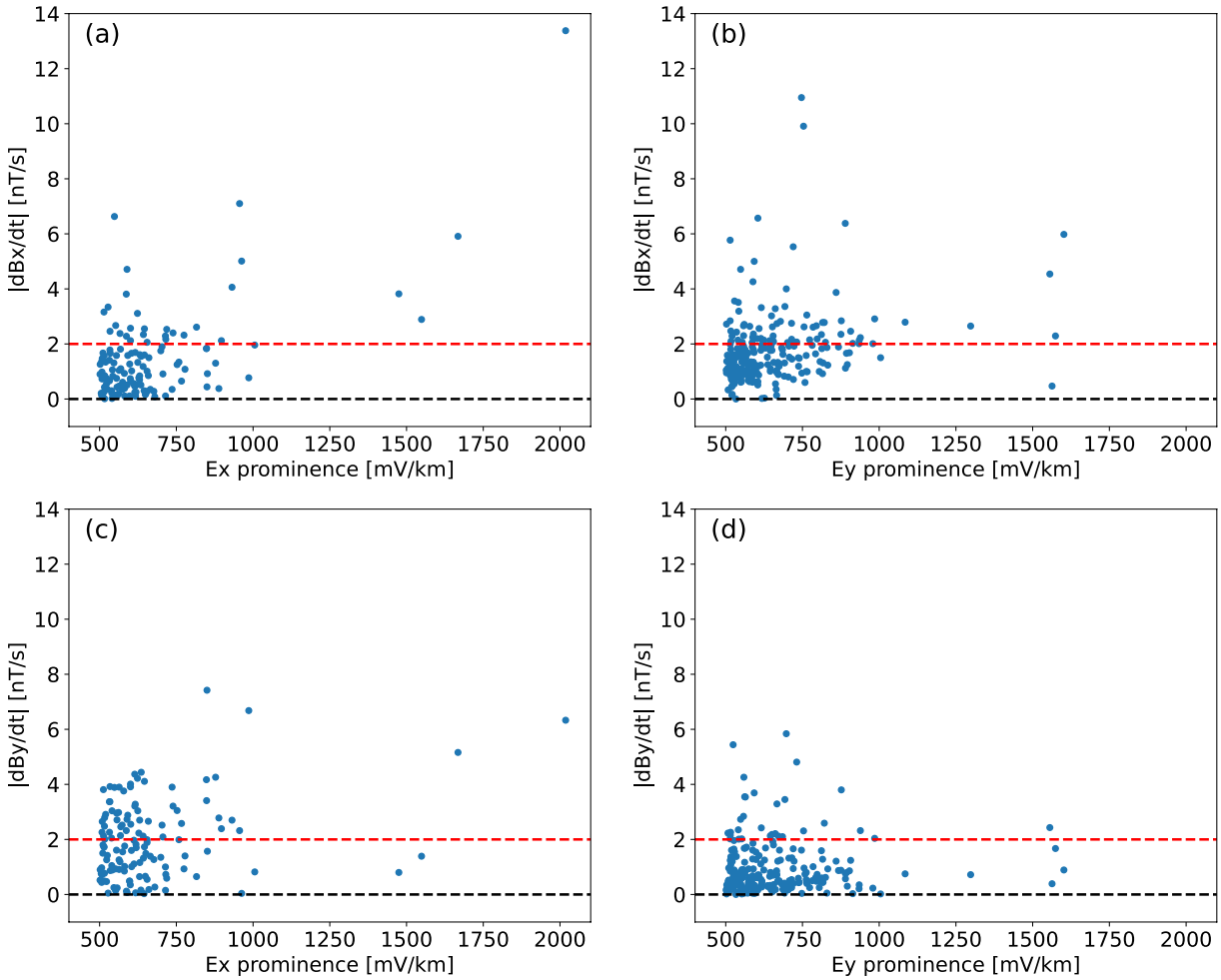

Figure 5. Distribution of $|dB_x/dt|$ (top panels) and $|dB_y/dt|$ (bottom panels) associated with intense geoelectric field events versus prominence for the E_x component (left) and the E_y component (right). The red and black horizontal dashed lines indicate the $|dB/dt|$ of 2 nT/s and 0 nT/s, respectively.

means we would expect to get very small prominences in the E_x component and very large prominences in the E_y component. However, our results show that more realistic models for IP shocks with an elliptically polarized B, and more realistic Earth conductivity that is inhomogeneous, will produce a mix of prominences in E_x and E_y components (Figure 4).

4.2. IMF Turning

A recent study by Tsurutani and Hajra (2021) showed that IMF northward and southward turnings are one cause of intense GICs at the Mäntsälä, Finland gas pipeline. In this study, we also found two storms with intense geoelectric fields associated with IMF turnings as shown in Table 2. Figure 9 shows one example that also occurred during the 24–25 October 2011 storm. The IMF rotated from southward (negative B_z) to duskward (positive B_y, Figure 9a), corresponding to the start of the recovery phase of the geomagnetic storm (Figure 7h). The MNE35 site was located at MLT ~19 hr when intense geoelectric fields were observed between 01:25 and 01:35 UT in response to this IMF turning (Figures 9c-9d). The time delay between the IMF turning from OMNI and the first intense geoelectric field peak observed around dusk is ~12 min, which is consistent with the reconfiguration timescales of ionospheric convection in response to IMF turnings (e.g., Murr & Hughes, 2001). Large magnetic field perturbations (ΔB ~300 nT) were also observed between 01:25 and 01:35 UT in Figures 9e-9f. The intense geoelectric fields and geomagnetic field perturbations were likely produced by a current system/convection reconfiguration in response to the IMF turning, although further analysis of multi-point ground and space-based observations is needed to confirm this. Note that IMF turnings can sometimes trigger substorms, and we can see

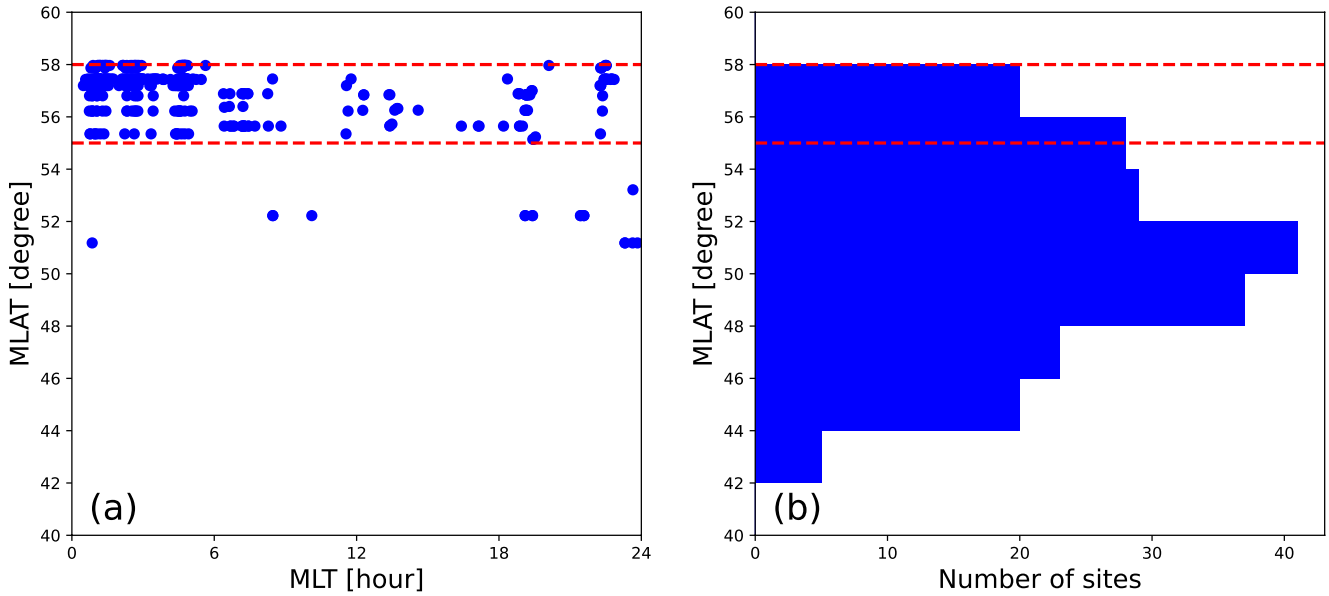

Figure 6. (a) Magnetic latitude (MLAT) versus magnetic local time distribution of intense geoelectric field events during storms. (b) Histogram of the number of EarthScope sites during 16 storms as a function of MLAT. The red horizontal dashed lines from top to bottom indicate MLAT of 58° and 55°, respectively.

the gradual increase of the AE index after the IMF turning in Figure 9g. However, the intense geoelectric fields were only observed at dusk during relatively low AE index (<450 nT) between 01:25 UT and 01:35 UT rather than when the AE index increased to 800 nT at 01:45 UT. We therefore attribute the source of this event as IMF turning instead of substorms.

Also noteworthy is the fact that small-scale ULF waves were superposed within the positive and negative bays in two horizontal magnetic field time series (Figures 9e–9f). Similar structures were also observed in the geoelectric fields, that is, shorter period waves embedded in longer period perturbations. Thus this event could potentially fit in the ULF wave category as well. A clearer example of ULF waves during the same time interval from the MND38 site is shown in Figure S1 in Supporting Information S1. Due to the superposition of perturbations with different periods, five peaks were identified in the two horizontal geoelectric field time series as shown in Figures 9c–9d. The largest prominence of the peaks is 1,500 mV/km. The geoelectric field peak associated $|dB_x/dt|$ values (varying from 2.3 to 5.0 nT/s) are consistently larger than the $|dB_y/dt|$. In total, five EarthScope sites observed intense geoelectric fields during this time interval. Another example from the MND35 site has already been shown in Figures 2b and 2c (zoomed in) and Figure 7 (zoomed out). Due to heterogeneous Earth conductivity, the geoelectric field response from five different sites separated from each other by distances ranging from 70 to 400 km are different although the geomagnetic field perturbations are similar, which is consistent with previous studies (Bedrosian & Love, 2015; Hartinger et al., 2020).

4.3. Substorm

Large geoelectric and geomagnetic field perturbations and GICs have long been reported to be associated with substorms. In this study, most of the intense geoelectric fields in this category were impulsive events and irregular pulsations that occurred during large AE index intervals on the nightside, which are most likely related to substorms. Figure 10 shows an example of intense geoelectric fields observed at site MNC35 during substorms on 15 July 2012 during the main phase of the geomagnetic storm. The largest peak prominence (1,600 mV/km) was detected in the E_y component at 07:44:17 UT with the corresponding $dB_x/dt = -5.98$ nT/s and $dB_y/dt = 0.89$ nT/s. Note that a few spikes in the E_y component indicated as magenta stars in Figure 10d are artifacts due to bad data values similar to the one shown as a magenta star in Figure 2b. These artifacts were visually inspected and removed from the statistical analysis presented in Section 3. In total, there are 14 EarthScope sites available in Minnesota and Iowa on this date. Eight sites observed similar impulses between 07 and 12 UT. As shown in Figure 10, these events are usually detected by multiple sites and grouped together in time

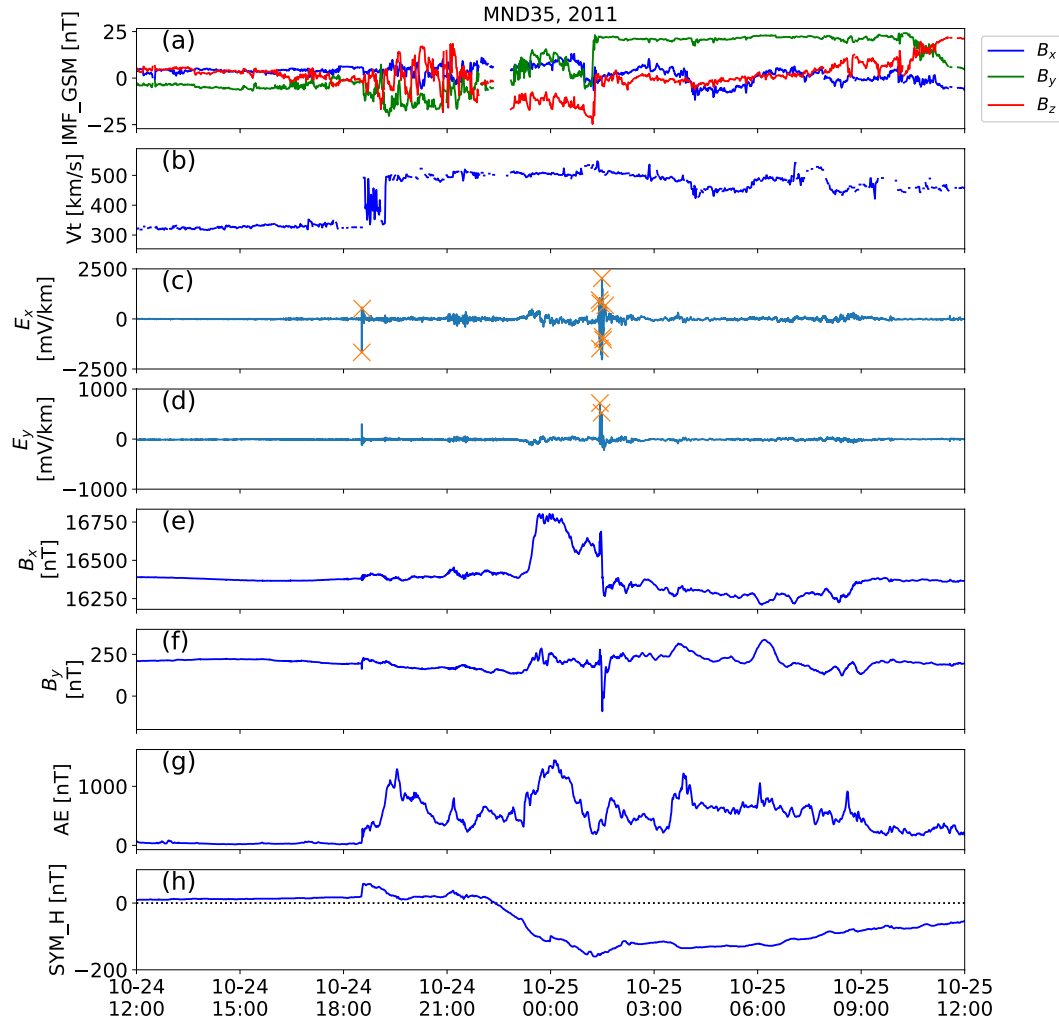

Figure 7. Interplanetary parameters and geomagnetic indices associated with intense geoelectric field events from site MND35 during the 24–25 October 2011 storm. From top to bottom: (a) interplanetary magnetic field in Geocentric solar magnetospheric coordinates; (b) solar wind velocity; (c) the north-south component of geoelectric fields observed at site MND35; (d) the east-west component of geoelectric fields observed at site MND35; (e) the north-south component of geomagnetic fields observed at site MND35; (f) the east-west component of geomagnetic fields observed at site MND35; (g) AE index; and (h) SYM-H index. Orange crosses are identified geoelectric field peaks.

during substorms. The first group of intense geoelectric fields observed between 07:20 and 08:20 UT are shown in Figure S2 in Supporting Information S1, in which geoelectric field impulses and irregular pulsations can be clearly seen. The driving mechanisms for these nightside intense geoelectric fields may vary from event to event and likely include large-scale auroral electrojets and localized current structures (Apatenkov et al., 2020; Belakhovsky et al., 2018, 2019; Engebretson et al., 2019), but definitive identification of the specific driver(s) in this case is beyond the scope of this study.

4.4. ULF Wave

The information presented in Table 2 shows ULF (1 mHz to 1 Hz) waves are one of the most common sources of intense geoelectric fields and have been detected in four out of six geomagnetic storms. One example of intense geoelectric fields driven by ULF waves during the 28 May 2017 storm is shown in Figure 11. Long period quasi-sinusoidal waves can be clearly seen in the geoelectric and geomagnetic field time series (Figures 11c–11f). These waves have been reported by Wang et al. (2020) as storm time Pc5 ULF pulsations observed by the Poker Flat Incoherent Scatter Radar and ground magnetometers. Our detection algorithm is able to detect several peaks

Table 2
Summary of Possible Sources of Intense Geoelectric Fields During Six Geomagnetic Storms

Storm date (Dst_{min})	IP shock C1	IMF turning C2	Substorm C3	ULF wave C4	Others C5
2011-09-26	09–26/12:36	09–26/19:37		09–26/12:39	09–26/20:54
(−118 nT)	MLT: 6.4 hr	MLT: 13.4 hr		MLT: 6.4 hr	MLT: 14.6 hr
2011-10-25	10–24/18:31	10–25/01:30		10–24/18:32	
(−147 nT)	MLT: 12.3 hr	MLT: 19.2 hr		MLT: 12.3 hr	
2012-07-15	07–14/18:12		07–15/07:00–12:00	07–15/04:58	07–15/00:43
(−139 nT)	MLT: 11.6 hr		MLT: 0–5 hr	MLT: 22.3	MLT: 18.4 hr
2013-06-29			06–29/04:00–12:00		
(−102 nT)			MLT: 22-06 hr		
2017-05-28				05–28/03:00–05:00	
(−125 nT)				MLT: 23-01 hr	
2017-09-08	09-07/23:02		09-08/00:00–02:00		09-08/13:00–15:00
(−124 nT)	MLT: 16.4 hr		MLT: 19–21 hr		MLT: 6.3–8.3 hr

and valleys of the waves when their prominences exceeded the 500 mV/km threshold. Unlike more transient peaks associated with IP shocks and substorms, the geoelectric field peaks associated with ULF waves during this storm have smaller prominence ($\leq$1,000 mV/km), longer width (a few hundred seconds), and smaller dB/dt (on the order of 0.1 nT/s).

ULF wave activity as a source of intense geoelectric fields has one characteristic that sets it apart from the other sources. Specifically, ULF waves can directly drive geomagnetic and electric perturbations while the other three sources are more or less indirect sources that are related to intense geoelectric fields through several possible mechanisms. Using the IP shock as an example, it is the IP shock generated sudden enhancement of the magnetopause current and field-aligned currents that drive geomagnetic perturbations, which in turn induce geoelectric fields, rather than the IP shock directly. Definitive identification of sources is challenging because intense geoelectric fields are sometimes associated with multiple sources simultaneously. For example, ULF waves can be driven by IP shocks and substorm activity (Oliveira et al., 2020; D. Zhang et al., 2020; James et al., 2013). The second geoelectric field peak in the E_x component in Figure 8c is associated with ULF waves driven by the IP shock. The intention of this paper is not to distinguish different sources on a case-by-case basis; rather, our aim is to provide improved understanding of which sources may be most prevalent during geomagnetic storms and highlight the considerable variability in the causes of intense geoelectric fields due to dependence on multiple factors, such as surface impedance and local time.

5. Discussion

Using 1-s geoelectric field measurements collected across the United States, we have investigated characteristics and sources of intense geoelectric fields with prominences of at least 500 mV/km that occurred during six separate geomagnetic storms. This multi-storm, multi-station analysis using direct geoelectric field measurements reveals new insights into the causes of extreme geoelectric fields. First, it is not straightforward to classify the sources of intense geoelectric fields because, sometimes, more than one mechanism contributes. Past studies tended to associate intense geoelectric fields/GICs with drivers that are one step removed from the geomagnetic fields that induce the geoelectric fields, such as IP shocks and IMF turnings that drive M-I currents/waves, which in turn couple to geomagnetic and geoelectric fields (e.g., Tsurutani & Hajra, 2021). This is an oversimplification and can potentially cause us to miss other very important factors that contribute to the geoelectric fields. For example, the IP shock and IMF turning in this study trigger waves seen in geomagnetic fields, and these are what lead to some intense geoelectric fields. We need to consider the intermediate steps - that is, the specific current systems/waves driven by the IP shocks/IMF turning/substorms - to better model and predict extreme geoelectric fields.

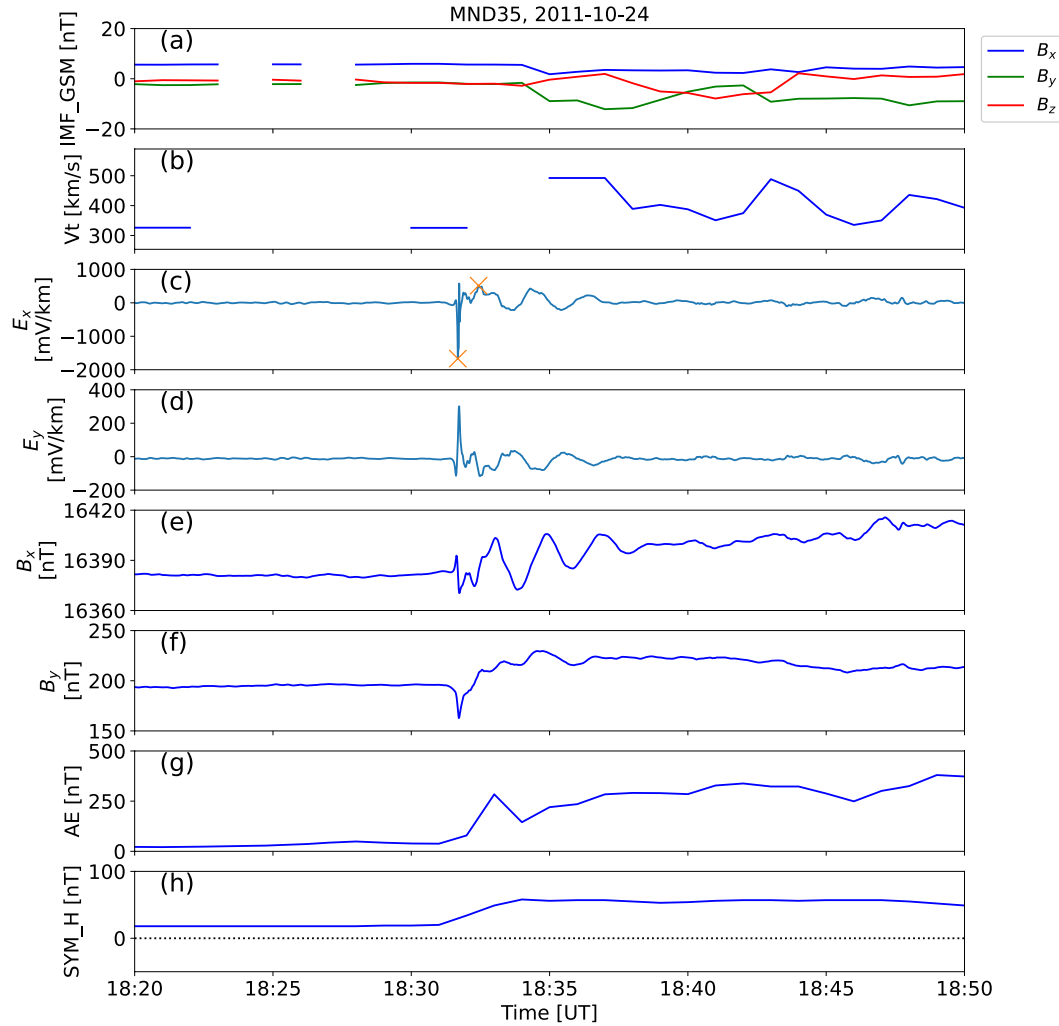

Figure 8. Close-up in time of the intense geoelectric fields associated with the interplanetary shock as observed at site MND35.

The second insight is that intense geoelectric fields depend on both the magnetosphere/ionosphere source and surface impedance as shown in Table 1 and Figure 6. We use the 2015 June null event storm shown in Table 1 as an example. Because the EarthScope sites during this storm were mainly located at low latitudes and low resistive regions in Kentucky and Tennessee, no intense geoelectric field was observed even though it was the strongest storm ($Dst_{\min} = -204$ nT) among the 16 storms we have surveyed. One example as observed at site TNV47 is shown in Figure 12. At the main phase of this storm, large magnetic perturbations were observed (Figures 12e–12f) at site TNV47, but the geoelectric field perturbations were relatively small (<500 *mV/km*) due to surface impedance and thus not detected by our algorithm. (Note that there exist a few geoelectric field peaks above 500 mV/km on June 24 and 27. These are spikes due to bad data values with a peak width less than 3 s (Figure S3 in Supporting Information S1) and thus were not detected by our algorithm.) This is related to our finding that most intense geoelectric fields are constrained to resistive regions where MLAT ≥55° during storms for which $-200\ nT \le Dst_{\min} \le -100\ nT$ (Figures 3b and 6a). A similar latitude threshold boundary in horizontal geomagnetic field and the induced geoelectric field fluctuations has also been reported by previous studies (e.g., Ngwira et al., 2013; Pulkkinen et al., 2012; Rogers et al., 2020), which is likely related to the maximum possible extent of equatorward expansion of the auroral electrojet current system. Note that more extreme storms ($Dst_{\min} < -200\ nT$) could push the auroral zone farther south, which may result in some intense geoelectric fields being observed beyond the latitude threshold identified in this study.

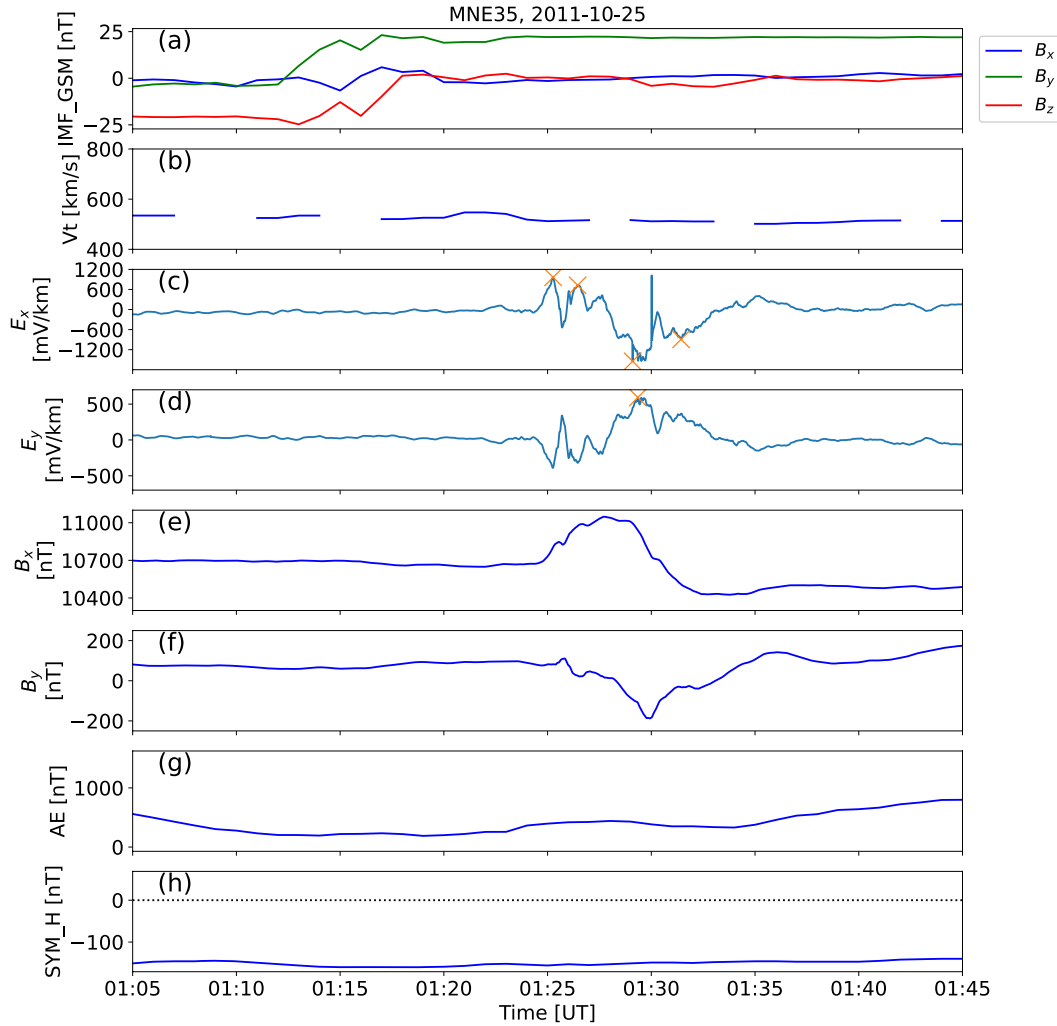

Figure 9. Similar to Figure 7, but for intense geoelectric fields associated with an interplanetary magnetic field turning and observed at site MNE35.

This study also shows that the sources of intense geoelectric fields differ from storm to storm (Table 2). This introduces another factor that affects the measured geoelectric fields: the location of observations relative to the source. Some sources have stronger impacts on the dayside (e.g., IP shocks and IMF turnings) and some on the nightside (e.g., substorms). Also, some sources have a global impact whereas others are more regional. One site can easily miss geoelectric impulses generated by small-scale currents during substorms if the site was located on the dayside or far away from the source region on the nightside. Although an IP shock can cause a global impact on the M-I coupled system (Belakhovsky et al., 2017), the response of a site located on the dayside and nightside at the same MLAT would be very different. Even if two sites were located at the same meridian on the dayside, the response at high latitudes and low latitudes would also be very different. All these factors contribute to the variability in the sources of intense geoelectric fields observed during geomagnetic storms and make the prediction of hazardous geoelectric fields and GICs challenging. These also lead to challenges in determining the most dominant source of intense geoelectric fields during geomagnetic storms. According to Table 2, both IP shocks and ULF waves occurred during four out of six geomagnetic storms. However, intense geoelectric fields occurring during substorms are usually detected by multiple sites and grouped together in time (Figure 10). We do not count the number of events for each category since it is challenging to distinguish between different sources and multiple sources can occur simultaneously. Future data analysis and modeling work is needed to quantitatively determine the most common source.

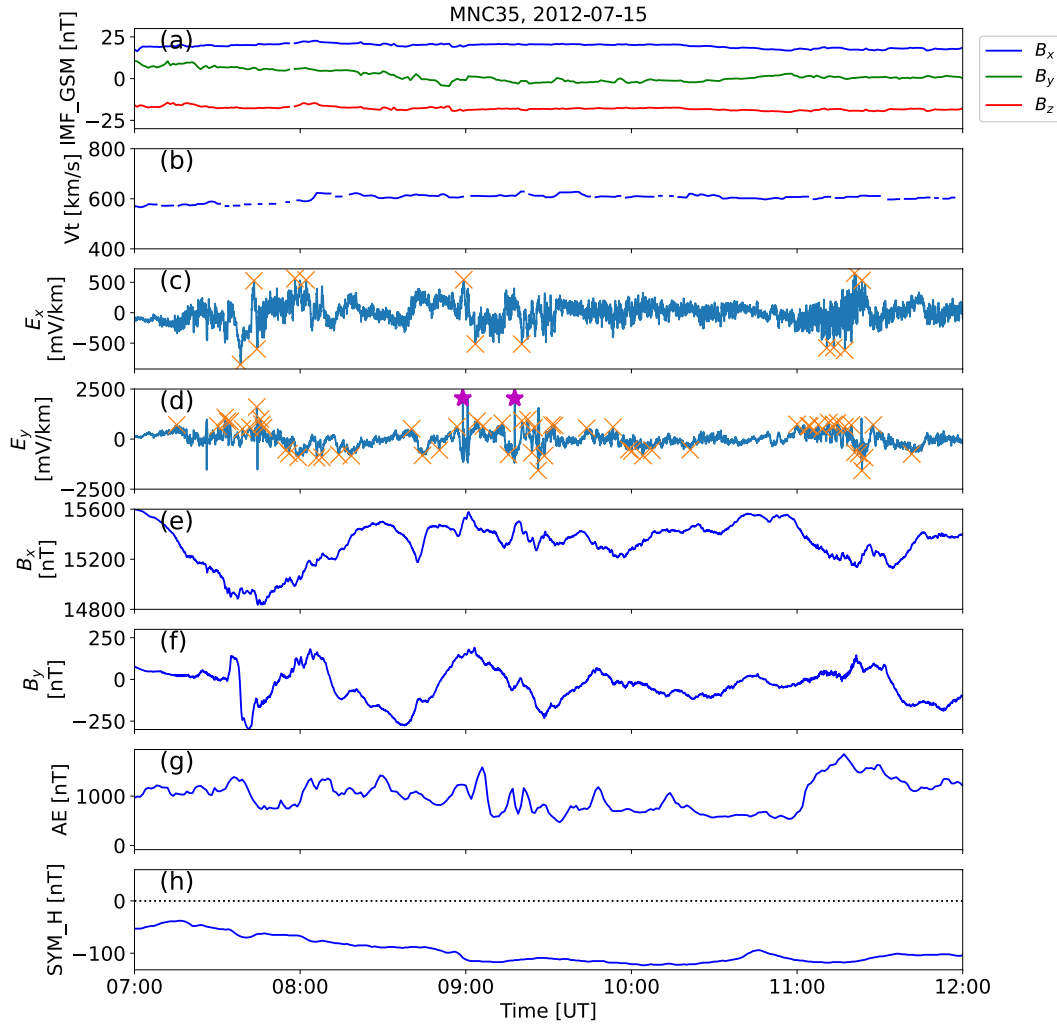

Figure 10. Similar to Figure 7, but for intense geoelectric fields observed during substorms at site MNC35.

Another point we would like to emphasize is the unique role of ULF wave activity as a direct driver of intense geoelectric fields during geomagnetic storms. Note that the drivers of ULF waves vary from external sources such as IP shocks to internal sources such as particle injections during substorms (Shi et al., 2018, 2020). However, these external and internal sources can also drive intense geoelectric fields via mechanisms other than ULF waves. Note that compared to the other mechanisms discussed, long-period ULF waves have sustained peak geoelectric fields and thus may have a relatively stronger impact on infrastructure. For the 28 May 2017 storm, as shown in Table 2, Pc5 ULF waves lasting for a few hours (Figure 11) are the only identified source to drive intense geoelectric fields at the EarthScope sites located in the northeast region of the United States. It has been shown that ULF waves are capable of driving intense geoelectric fields of ∼1,000 mV/km at mid-latitudes during moderate storms (Hartinger et al., 2020). In extreme cases during strong geomagnetic storms (e.g., the 2003 Halloween storm), it is believed that ULF waves can drive hazardous geoelectric fields and GICs (Heyns et al., 2021).

While past studies examining storm-time geoelectric fields based on observations from one station or during a single storm, this study indicates that multiple factors need to be taken into account based on comparative analysis of intense geoelectric fields during multiple geomagnetic storms. One novel piece of this investigation is the use of a large number of EarthScope sites across the United States that enables us to sample many geographic regions (and various geologic settings) during multiple geomagnetic storms and at high time resolution. Previous statistical studies have tended to use 1-min resolution geoelectric and geomagnetic field data, which likely missed certain types of events such as ULF waves with periods on the order of 1–2 min or less

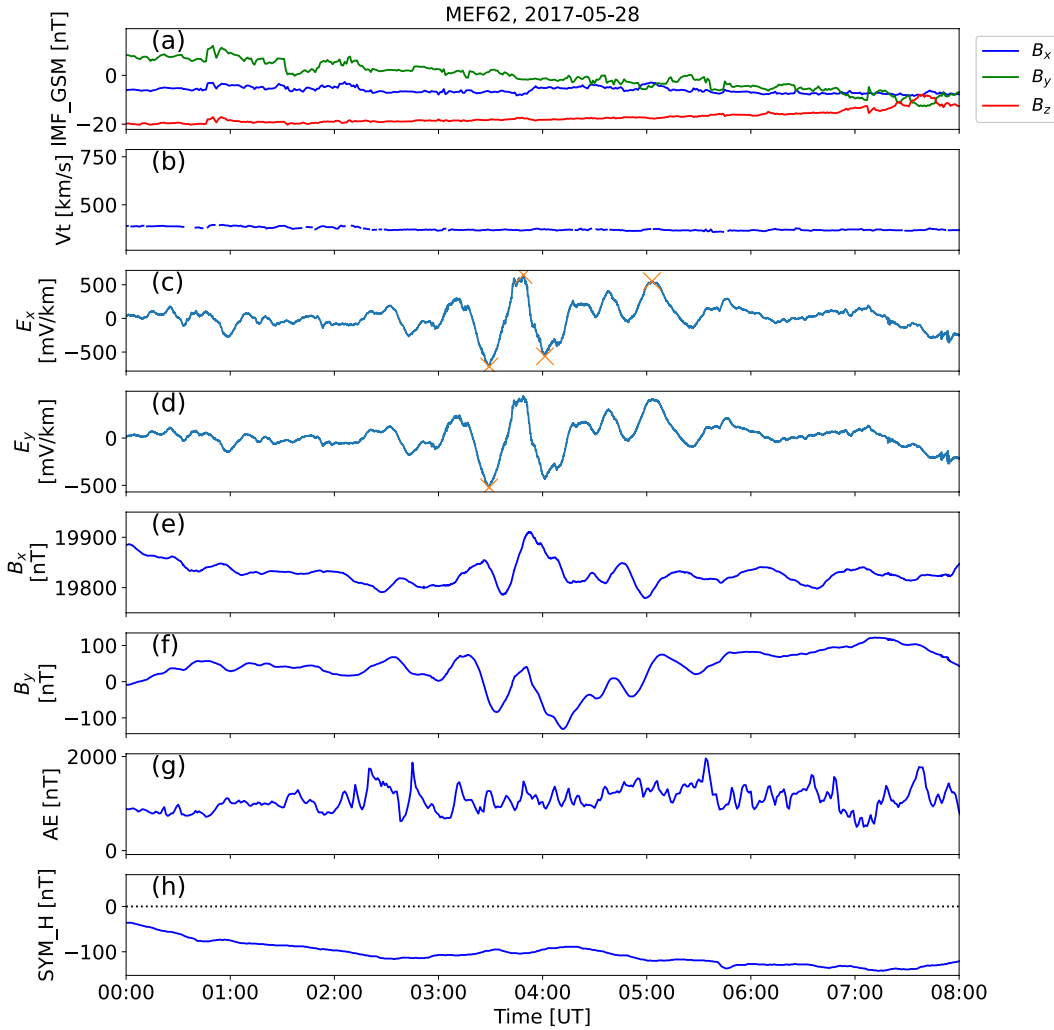

Figure 11. Similar to Figure 7, but for intense geoelectric fields associated with ultralow frequency waves and observed at site MEF62.

(Figures 8, 9, and S1 in Supporting Information S1) and impulses with a duration less than 1 min (Figure 8). Our study indicates intense short-lived and/or high frequency geoelectric field events are quite common. From the operational point of view (e.g., NOAA Space Weather Prediction Center), producing 1-min geoelectric or geomagnetic field data is more practical and efficient for the purpose of prediction. However, in order to make the prediction more accurate, improve models would be needed to capture missing physics and to increase the temporal and spatial resolution. For example, in predictive models of extreme geoelectric fields, based on our analysis of these events, 3D Earth conductivity and realistic model of current systems driven by IP shocks and IMF turnings would ideally be taken into account. Such effort has been made by NOAA to generate geoelectric field maps with a recently upgraded 3D empirical conductivity model (https://www.swpc.noaa.gov/news/geoelectric-field-map-upgrade-3d-empirical-conductivity-model). As pointed out in Ngwira et al. (2015) and Hartinger et al. (2020), it is challenging to identify the processes that drive extreme geoelectric fields. An interdisciplinary community-wide effort involving the MT, space science data analysis, space weather modeling, and the power system engineering communities would be beneficial to advance our understanding of hazardous geoelectric fields and GICs.

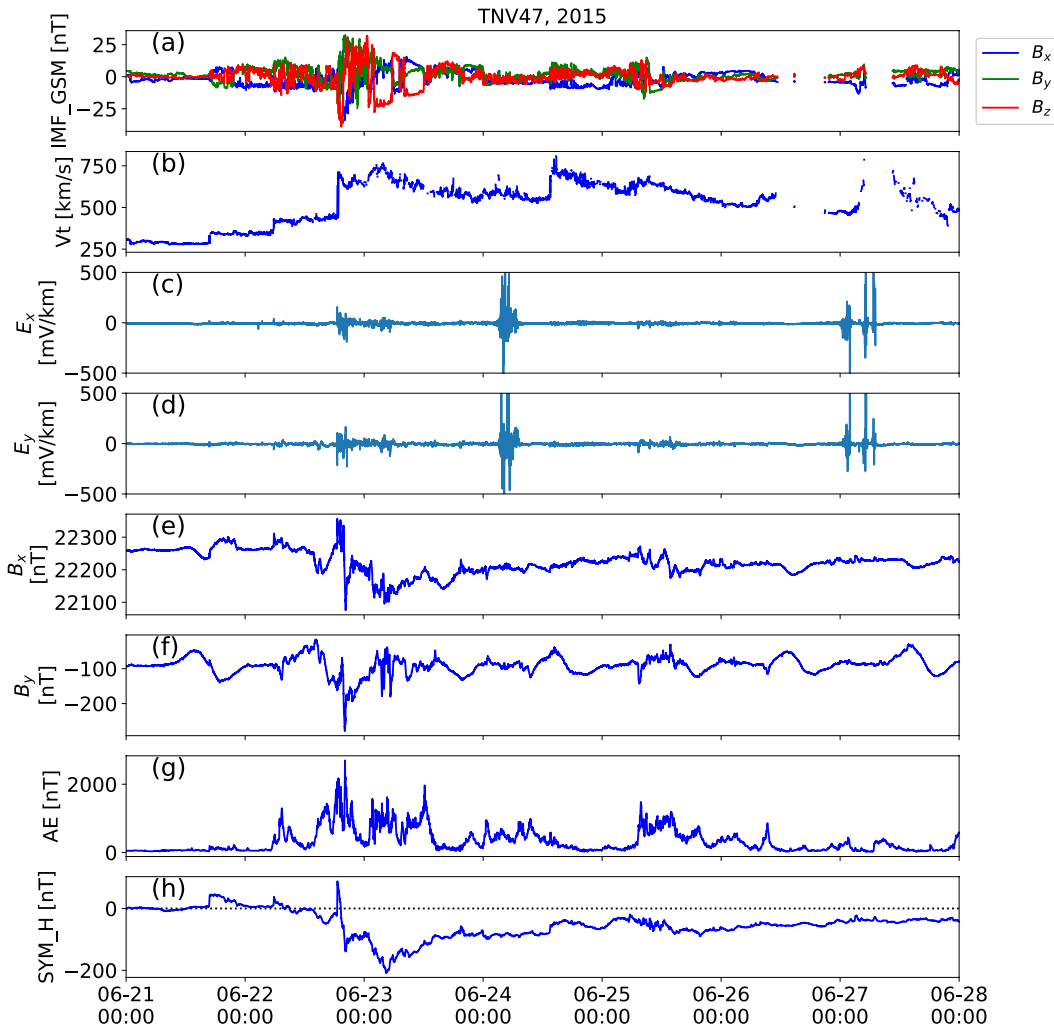

Figure 12. Similar to Figure 7, but for geoelectric fields observed at site TNV47.

6. Conclusions

In summary, an algorithm was applied to directly measured 1-s geoelectric field data from 203 EarthScope sites during 16 geomagnetic storms to find temporally localized peaks. Most of the intense geoelectric field peaks were observed in resistive regions with MLATs greater than 55°. Various sources of intense geoelectric fields have been identified during geomagnetic storms, namely, IP shocks, IMF turnings, substorms, and ULF waves. The sources of intense geoelectric fields differ from storm to storm. This is likely because the generation of geoelectric fields depends on multiple factors including regional Earth conductivity, sources from the solar wind and M-I system, as well as the location of observations relative to these sources. Extreme geoelectric fields related to these sources can have amplitudes of 1,000–2000 mV/km, comparable to the thresholds commonly used to identify hazardous events.

Data Availability Statement

The Dst data used in this paper was provided by the World Data Center for Geomagnetism, Kyoto (http://wdc.kugi.kyoto-u.ac.jp/dstdir/index.html). The event list with information on the properties of identified intense geoelectric fields can be found in Zenodo (https://doi.org/10.5281/zenodo.6338092). The OMNI data were obtained from the GSFC/SPDF OMNIWeb interface at https://omniweb.gsfc.nasa.gov.

Acknowledgments
MDH and XS are supported by NASA award 80NSSC19K0907. JB is supported by NSF award AGS-2027168. BSM is supported by a Mendenhall Postdoctoral Fellowship through the U.S. Geological Survey. We acknowledge Christopher Balch and Wenbin Wang for internal review. We acknowledge bezpy (https://doi.org/10.5281/zenodo.3765861) for loading EarthScope data and pyspedas for loading OMNI and geomagnetic index data. USArray MT TA project was led by Principal Investigator Adam Schultz and Gary Egbert. USArray TA was funded through NSF Grant EAR0323311, IRIS Subaward 478 and 489 under NSF Cooperative Agreement EAR0350030 and EAR0323309, IRIS Subaward 75 MT under NSF Cooperative Agreement EAR0733069 under CFDA 47.050, and IRIS Subaward 05OSUSAGE under NSF Cooperative Agreement EAR1261681 under CFDA 47.050. The facilities of IRIS Data Services, and specifically the IRIS Data Management Center, were used for access to waveforms, related metadata, and/or derived products used in this study (http://service.iris.edu/irisws/timeseries/1/). IRIS Data Services are funded through the Seismological Facilities for the Advancement of Geoscience (SAGE) Award of the National Science Foundation under Cooperative Support Agreement EAR-1851048. The National Center for Atmospheric Research is sponsored by the National Science Foundation. Any use of trade, firm, or product names is for descriptive purposes only and does not imply endorsement by the U.S. Government.

References

Apatenkov, S. V., Pilipenko, V. A., Gordeev, E. I., Viljanen, A., Juusola, L., Belakhovsky, V. B., et al. (2020). Auroral omega bands are a significant cause of large geomagnetically induced currents. *Geophysical Research Letters*, *47*(6), e2019GL086677. Retrieved from https://agupubs.onlinelibrary.wiley.com/doi/abs/10.1029/2019GL086677

Arritt, B. (2020). *Furthering the understanding of the characteristics and scales of geoelectric field enhancements*. 3002017900. EPRI.

Bedrosian, P. A. (2016). Making it and breaking it in the midwest: Continental assembly and rifting from modeling of earthscope magnetotelluric data. *Precambrian Research*, *278*, 337–361. Retrieved from https://www.sciencedirect.com/science/article/pii/S0301926816300225

Bedrosian, P. A., & Love, J. J. (2015). Mapping geoelectric fields during magnetic storms: Synthetic analysis of empirical United States impedances. *Geophysical Research Letters*, *42*(23), 10–160. https://doi.org/10.1002/2015GL066636

Belakhovsky, V., Pilipenko, V., Engebretson, M., Sakharov, Y., & Selivanov, V. (2019). Impulsive disturbances of the geomagnetic field as a cause of induced currents of electric power lines. *Journal of Space Weather and Space Climate*, *9*, A18. https://doi.org/10.1051/swsc/2019015

Belakhovsky, V., Pilipenko, V., Sakharov, Y. A., Lorentzen, D., & Samsonov, S. (2017). Geomagnetic and ionospheric response to the interplanetary shock on January 24, 2012. *Earth Planets and Space*, *69*. 105. https://doi.org/10.1186/s40623-017-0696-1

Belakhovsky, V., Pilipenko, V., Sakharov, Y. A., & Selivanov, V. (2018). Characteristics of the variability of a geomagnetic field for studying the impact of the magnetic storms and substorms on electrical energy systems. *Izvestiya - Physics of the Solid Earth*, *54*(1), 52–65. https://doi.org/10.1134/s1069351318010032

Berdichevsky, M., & Dmitriev, V. (1976). Distortion of magnetic and electric field by near-surface lateral inhomogeneities. *Acta Geodaetica, Geophysica et Montanistica Hungarica*, *11*, 447–483.

Blanch, E., Marsal, S., Segarra, A., Torta, J. M., Altadill, D., & Curto, J. J. (2013). Space weather effects on earth's environment associated to the 24–25 October 2011 geomagnetic storm. *Space Weather*, *11*(4), 153–168. Retrieved from https://agupubs.onlinelibrary.wiley.com/doi/abs/10.1002/swe.20035

Engebretson, M. J., Pilipenko, V. A., Ahmed, L. Y., Posch, J. L., Steinmetz, E. S., Moldwin, M. B., et al. (2019). Night time magnetic perturbation events observed in arctic Canada: 1. Survey and statistical analysis. *Journal of Geophysical Research: Space Physics*, *124*(9), 7442–7458. Retrieved from https://agupubs.onlinelibrary.wiley.com/doi/abs/10.1029/2019JA026794

Espinosa, K. V., Padilha, A. L., & Alves, L. R. (2019). Effects of ionospheric conductivity and ground conductance on geomagnetically induced currents during geomagnetic storms: Case studies at low-latitude and equatorial regions. *Space Weather*, *17*(2), 252–268. Retrieved from https://agupubs.onlinelibrary.wiley.com/doi/abs/10.1029/2018SW002094

Freeman, M. P., Forsyth, C., & Rae, I. J. (2019). The influence of substorms on extreme rates of change of the surface horizontal magnetic field in the United Kingdom. *Space Weather*, *17*(6), 827–844. Retrieved from https://agupubs.onlinelibrary.wiley.com/doi/abs/10.1029/2018SW002148

Gil, A., Berendt-Marchel, M., Modzelewska, R., Moskwa, S., Siluszyk, A., Siluszyk, M., et al. (2021). Evaluating the relationship between strong geomagnetic storms and electric grid failures in Poland using the geoelectric field as a gic proxy. *Journal of Space Weather and Space Climate*, *11*. https://doi.org/10.1051/swsc/2021013

Hartinger, M. D., Shi, X., Lucas, G. M., Murphy, B. S., Kelbert, A., Baker, J. B. H., et al. (2020). Simultaneous observations of geoelectric and geomagnetic fields produced by magnetospheric ulf waves. *Geophysical Research Letters*, *47*(18), e2020GL089441. Retrieved from https://agupubs.onlinelibrary.wiley.com/doi/abs/10.1029/2020GL089441

Heyns, M. J., Lotz, S. I., & Gaunt, C. T. (2021). Geomagnetic pulsations driving geomagnetically induced currents. *Space Weather*, *19*(2), e2020SW002557. Retrieved from https://agupubs.onlinelibrary.wiley.com/doi/abs/10.1029/2020SW002557

James, M. K., Yeoman, T. K., Mager, P. N., & Klimushkin, D. Y. (2013). The spatio-temporal characteristics of ulf waves driven by substorm injected particles. *Journal of Geophysical Research: Space Physics*, *118*(4), 1737–1749. Retrieved from https://agupubs.onlinelibrary.wiley.com/doi/abs/10.1002/jgra.50131

Joselyn, J. A., & Tsurutani, B. T. (1990). Geomagnetic sudden impulses and storm sudden commencements: A note on terminology. *Eos, Transactions American Geophysical Union*, *71*(47), 1808–1809. Retrieved from https://agupubs.onlinelibrary.wiley.com/doi/abs/10.1029/90EO00350

Kappenman, J. G. (2003). Storm sudden commencement events and the associated geomagnetically induced current risks to ground-based systems at low-latitude and midlatitude locations. *Space Weather*, *1*(3). Retrieved from https://agupubs.onlinelibrary.wiley.com/doi/abs/10.1029/2003SW000009

Kelbert, A., Bedrosian, P. A., & Murphy, B. S. (2019). The first 3D conductivity model of the contiguous United States. In *Geomagnetically induced currents from the sun to the power grid* (pp. 127–151). American Geophysical Union (AGU). https://doi.org/10.1002/9781119434412.ch8

Lucas, G. M., Love, J. J., Kelbert, A., Bedrosian, P. A., & Rigler, E. J. (2020). A 100-year geoelectric hazard analysis for the U.S. High-voltage power grid. *Space Weather*, *18*(2), e2019SW002329. https://doi.org/10.1029/2019SW002329

Murphy, B. S., Lucas, G. M., Love, J. J., Kelbert, A., Bedrosian, P. A., & Rigler, E. J. (2021). Magnetotelluric sampling and geoelectric hazard estimation: Are national-scale surveys sufficient? *Space Weather*, *19*(7), e2020SW002693. Retrieved from https://agupubs.onlinelibrary.wiley.com/doi/abs/10.1029/2020SW002693

Murr, D. L., & Hughes, W. J. (2001). Reconfiguration timescales of ionospheric convection. *Geophysical Research Letters*, *28*(11), 2145–2148. Retrieved from https://agupubs.onlinelibrary.wiley.com/doi/abs/10.1029/2000GL012765

Ngwira, C. M., Pulkkinen, A., Wilder, F. D., & Crowley, G. (2013). Extended study of extreme geoelectric field event scenarios for geomagnetically induced current applications. *Space Weather*, *11*(3), 121–131. Retrieved from https://agupubs.onlinelibrary.wiley.com/doi/abs/10.1002/swe.20021

Ngwira, C. M., Pulkkinen, A. A., Bernabeu, E., Eichner, J., Viljanen, A., & Crowley, G. (2015). Characteristics of extreme geoelectric fields and their possible causes: Localized peak enhancements. *Geophysical Research Letters*, *42*(17), 6916–6921. Retrieved from https://agupubs.onlinelibrary.wiley.com/doi/abs/10.1002/2015GL065061

Oliveira, D. M., Hartinger, M. D., Xu, Z., Zesta, E., Pilipenko, V. A., Giles, B. L., & Silveira, M. V. D. (2020). Interplanetary shock impact angles control magnetospheric ulf wave activity: Wave amplitude, frequency, and power spectra. *Geophysical Research Letters*, *47*(24), e2020GL090857. Retrieved from https://agupubs.onlinelibrary.wiley.com/doi/abs/10.1029/2020GL090857

Pulkkinen, A., Bernabeu, E., Eichner, J., Beggan, C., & Thomson, A. W. P. (2012). Generation of 100-year geomagnetically induced current scenarios. *Space Weather*, *10*(4). Retrieved from https://agupubs.onlinelibrary.wiley.com/doi/abs/10.1029/2011SW000750

Pulkkinen, A., Bernabeu, E., Thomson, A., Viljanen, A., Pirjola, R., Boteler, D., et al. (2017). Geomagnetically induced currents: Science, engineering, and applications readiness. *Space Weather*, *15*(7), 828–856. https://doi.org/10.1002/2016SW001501

Rogers, N. C., Wild, J. A., Eastoe, E. F., Gjerloev, J. W., & Thomson, A. W. P. (2020). A global climatological model of extreme geomagnetic field fluctuations. *Journal of Space Weather and Space Climate*, *10*. https://doi.org/10.1051/swsc/2020008

Schultz, A. (2010). Emscope: A continental scale magnetotelluric observatory and data discovery resource. *Data Science Journal*, *8*, IGY6–IGY20. https://doi.org/10.2481/dsj.ss_igy-009

Shi, X., Baker, J. B. H., Ruohoniemi, J. M., Hartinger, M. D., Murphy, K. R., Rodriguez, J. V., et al. (2018). Long-lasting poloidal ULF waves observed by multiple satellites and high-latitude SuperDARN radars. *Journal of Geophysical Research: Space Physics*, *123*(10), 8422–8438. Retrieved from https://agupubs.onlinelibrary.wiley.com/doi/abs/10.1029/2018JA026003

Shi, X., Hartinger, M. D., Baker, J. B. H., Ruohoniemi, J. M., Lin, D., Xu, Z., et al. (2020). Multipoint conjugate observations of dayside ULF waves during an extended period of radial IMF. *Journal of Geophysical Research: Space Physics*, *125*(11), e2020JA028364. Retrieved from https://agupubs.onlinelibrary.wiley.com/doi/abs/10.1029/2020JA028364

Tsurutani, B. T., & Hajra, R. (2021). The interplanetary and magnetospheric causes of geomagnetically induced currents (GICs) > 10 A in the Mäntsälä Finland pipeline: 1999 through 2019. *Journal of Space Weather and Space Climate*, *11*, A2. https://doi.org/10.1051/swsc/2021001

Viljanen, A. (1997). The relation between geomagnetic variations and their time derivatives and implications for estimation of induction risks. *Geophysical Research Letters*, *24*(6), 631–634. Retrieved from https://agupubs.onlinelibrary.wiley.com/doi/abs/10.1029/97GL00538

Virtanen, P., Gommers, R., Oliphant, T. E., Haberland, M., Reddy, T., Cournapeau, D., et al. (2020). SciPy 1.0: Fundamental algorithms for scientific computing in Python. *Nature Methods*, *17*(3), 261–272. https://doi.org/10.1038/s41592-019-0686-2

Wang, B., Nishimura, Y., Hartinger, M., Sivadas, N., Lyons, L. L., Varney, R. H., & Angelopoulos, V. (2020). Ionospheric modulation by storm time pc5 ulf pulsations and the structure detected by pfisr-themis conjunction. *Geophysical Research Letters*, *47*(16), e2020GL089060. Retrieved from https://agupubs.onlinelibrary.wiley.com/doi/abs/10.1029/2020GL089060

Williams, M. L., Fischer, K. M., Freymueller, J. T., Tikoff, B., Tréhu, A. M., & others (2010). *Unlocking the secrets of the north American continent: An EarthScope science plan for 2010-2020*. EarthScope.

World Data Center for Geomagnetism, Kyoto, Nosé, M., Iyemori, T., Sugiura, M., & Kamei, T. (2015). Geomagnetic Dst index. https://doi.org/10.17593/14515-74000

Yagova, N. V., Pilipenko, V. A., Sakharov, Y. A., & Selivanov, V. N. (2021). Spatial scale of geomagnetic Pc5/Pi3 pulsations as a factor of their efficiency in generation of geomagnetically induced currents. *Earth Planets and Space*, *73*, 88. https://doi.org/10.1186/s40623-021-01407-2

Zhang, D., Liu, W., Li, X., Sarris, T. E., Wang, Y., Xiao, C., et al. (2020). Relation between shock-related impulse and subsequent ULF wave in the earth's magnetosphere. *Geophysical Research Letters*, *47*(23), e2020GL090027. Retrieved from https://agupubs.onlinelibrary.wiley.com/doi/abs/10.1029/2020GL090027

Zhang, J. J., Wang, C., Sun, T. R., Liu, C. M., & Wang, K. R. (2015). GIC due to storm sudden commencement in low-latitude high-voltage power network in China: Observation and simulation. *Space Weather*, *13*(10), 643–655. Retrieved from https://agupubs.onlinelibrary.wiley.com/doi/abs/10.1002/2015SW001263

Zhang, J. J., Yu, Y. Q., Wang, C., Du, D., Wei, D., & Liu, L. G. (2020). Measurements and simulations of the geomagnetically induced currents in low-latitude power networks during geomagnetic storms. *Space Weather*, *18*(8), e2020SW002549. Retrieved from https://agupubs.onlinelibrary.wiley.com/doi/abs/10.1029/2020SW002549

Zou, S., Ridley, A. J., Moldwin, M. B., Nicolls, M. J., Coster, A. J., Thomas, E. G., & Ruohoniemi, J. M. (2013). Multi-instrument observations of SED during 24–25 October 2011 storm: Implications for SED formation processes. *Journal of Geophysical Research: Space Physics*, *118*(12), 7798–7809. Retrieved from https://agupubs.onlinelibrary.wiley.com/doi/abs/10.1002/2013JA018860